The Effects of Ocean Surface Waves on Global Intraseasonal Prediction: Case Studies with a Coupled CFSv2.0-WW3 System

Ruizi Shi[1], Fanghua Xu[1*], Li Liu[1], Zheng Fan[1], Hao Yu[1], Hong Li[1,3], Xiang Li[2] and Yunfei Zhang[2]

[1] Ministry of Education Key Laboratory for Earth System Modeling, and Department of Earth System Science, Tsinghua University, Beijing, 100084, China

[2] Key Laboratory of Marine Hazards Forecasting, National Marine Environmental Forecasting Center, Ministry of Natural Resources, Beijing, 100081, China

[3] Department of Atmospheric and Oceanic Sciences and Institute of Atmospheric Sciences, Fudan University, Shanghai, 200433, China.

Correspondence to: Fanghua Xu (fxu@mail.tsinghua.edu.cn)

Abstract. This article describes the implementation of a coupling between a global forecast model (CFSv2.0) and a wave model (WW3), and investigates the effects of ocean surface waves on the air-sea interface in the new framework. Several major wave-related processes, including the Langmuir mixing, Stokes-Coriolis force with entrainment, air-sea fluxes modified by Stokes drift and momentum roughness length, are evaluated in two groups of 56-day experiments, one for boreal winter and the other for boreal summer. Comparisons are made against in-situ buoys, satellite measurements and reanalysis data, to evaluate the influence of waves on intraseasonal prediction of sea surface temperature (SST), 2-m air temperature (T02), mixed layer depth (MLD), 10-m wind speed (WSP10) and significant wave height (SWH). The wave-coupled experiments show that overestimated SSTs and T02s, as well as underestimated MLDs at mid-high latitudes in summer from original CFSv2.0 are significantly improved due to enhanced vertical mixing generated by Stokes drift. For WSP10s and SWHs, the wave-related processes generally reduce ~~lead to reduction of~~ biases in regions where WSP10s and SWHs are overestimated. On one hand, the decreased SSTs stabilize the marine atmospheric boundary layer, weaken WSP10s and then SWHs. On the other hand, the increased roughness length due to waves reduces ~~leads to reduction in~~ the originally overestimated WSP10s and SWHs. In addition, the effects of Stokes drift and current on air-sea fluxes also rectify WSP10s and SWHs. These cases are helpful for the future development of the two-way CFSv2.0-wave coupled system.

1 Introduction

Ocean surface gravity waves play an important role in modifying physical processes at the atmosphere–ocean interface, which can influence momentum, heat and freshwater fluxes across the air-sea interface (Li and Garrett, 1997; Taylor and Yelland, 2001; Moon et al., 2004; Janssen 2004; Belcher et al., 2012; Moum and Smyth, 2019). For instance, ocean surface waves modify ocean surface roughness to influence the marine atmospheric boundary layer and thus change the momentum, latent heat, and sensible heat transfer (Janssen 1989, 1991; Taylor and Yelland, 2001; Moon et al., 2004; Drennan et al., 2003, 2005). The breaking waves inject turbulent kinetic energy in the upper ocean, which enhances the mixing process (Terray et al. 1996). Nonbreaking surface waves also affect mixing in the upper ocean by adding a wave-related Reynolds stress (Qiao et al., 2004; Ghantous and Babanin, 2014). The wave-related Stokes drift interacts with Coriolis force and produces the Coriolis-Stokes force (Hasselmann 1970). The shear of Stokes drift is critical for generation of Langmuir circulation, which significantly deepens the mixed layer by strong vertical mixing both at climate scales (Li and Garrett 1997; Belcher et al., 2012) and at weather scales (Kukulka et al., 2009).

Various wave-related parameterizations have been proposed and ~~applied~~used in ~~modeling~~modelling. The wave-related Charnock parameter (C_{ch}) defines sea surface roughness and affects wind stress estimates (Pineau-Guillou et al. 2018; Sauvage et al. 2020). There are primarily three methods for defining C_{ch}, assessed from the wave-induced kinematic stress (Janssen 1989, 1991), the wave age (Drennan et al., 2003, 2005; Moon et al., 2004), or the steepness (Taylor and Yelland, 2001). The former two are based on the wind-sea conditions, whereas the latter includes both swells and wind-sea waves. Modifications to these Charnock parameterizations were suggested in recent studies for the leveling off roughness under high winds (~~e.g.~~e.g., Fan et al., 2012; Bidlot et al., 2020; ECMWF, 2020; Li et al., 2021).

56   In the oceanic boundary layer, waves influence upper ocean mixing via wave dissipation and Stokes

57   drift-induced processes. In Breivik et al. (2015), the wave dissipation-related turbulent kinetic energy

58   flux is found to yield the largest sea surface temperature (SST) differences in the extratropics. The Stokes

59   drift-induced Langmuir turbulence can improve temperature simulation over most of the world oceans,

60   particularly in the Southern Ocean (Belcher et al., 2012; Li et al., 2016). Polonichko (1997), Van Roekel

61   et al. (2012) and Li et al. (2017) indicated that the Langmuir cell intensity strongly depends on the

62   alignment of winds and waves, reaching maximum when they are aligned. Li et al. (2016) found the

63   effect of Langmuir cell can be further enhanced by entrainment. In Couvelard et al. (2020), the Stokes

64   drift- -related forces can also contribute modestly to the deepening of the mixed layer depth (MLD)

65   modestly. In the First Institute of Oceanography Earth System Model, Bao et al. (2019) indicated that

66   the non-breaking wave-induced mixing, Stokes drift-affected air-sea fluxes, as well as sea spray are all

67   important for climate estimates.

68   The wave-related processes at the air-sea interface are complex and important in global coupled

69   systems (e.g., Breivik et al. 2015; Law-Chune and Aouf, 2018; Bao et al. 2019; Couvelard et al. 2020).

70   Most of the coupled models with a wave component at global scale were developed for climate research

71   (e.g., Law-Chune and Aouf, 2018; Bao et al. 2019; Couvelard et al. 2020). Exceptionally, an Integrated

72   Forecasting System (IFS) with fully coupled atmosphere, ocean and wave components, developed by

73   European Centre for Medium-Range Weather Forecasts (ECMWF) (Janssen 2004; Bidlot et al. 2019,

74   2020), has been released with great flexibility for global forecasts from medium-range weather scales to

75   seasonal scales (Breivik et al. 2015).

76   The effects of wave-related processes are worth further evaluation in different global coupled

77   modelling systems. Since it takes sufficient periods for the wave energy to develop (Janssen 2004), we

78   investigate the impact of individual wave process at intraseasonal timescale in a new global atmosphere-

79   ocean-wave system. To achieve this, we coupled the WAVEWATCH III (WW3) to the Climate Forecast

80   System model version 2.0 (CFSv2.0) and then conducted sensitivity experiments in boreal winter and

81   summer for comparison. The effects of upper ocean mixing modified by Langmuir cell, Stokes-Coriolis

82   force and entrainment, air-sea fluxes modified by surface current and Stokes drift, and momentum

83   roughness length are evaluated. The CFSv2.0 is a coupled system with the main application for

84   intraseasonal and seasonal prediction (e.g.e.g., Saha et al. 2014). The National Centers for Environmental

85   Prediction (NCEP) is establishing its own atmosphere-ocean-wave system, in which the Global Forecast

86   System (GFS; the atmosphere module in CFSv2.0 system) is one-way coupled with WW3. Our work can

87   provide insights for two-way wave coupling of CFSv2.0, and is helpful for the future development of the

88   CFSv2.0-wave coupling system. Two groups of 56-day predictions were conducted for boreal winter and

89   boreal summer, respectively. Then, the predictions were then compared with observations and reanalysis

90   data. For each group, sensitivity experiments with different wave parameterizations were carried out to

91   evaluate the effects of individual wave-related process.

92   The rest of the paper is structured as follows: methods and numerical experiments with different

93   parameterizations are described in Section 2; the observations and reanalysis data are introduced in

94   Section 3, and the results of experiments are evaluated and compared in Section 4. Finally, a summary

95   and discussion are given in Section 5.

96   **2 Methods and Experiments**

97   **2.1 Coupling WAVEWATCH III with CFSv2.0**

98   The version 5.16 of WW3 (WAVEWATCH III Development Group, 2016) developed by the National

99   Oceanic and Atmospheric Administration (NOAA)/NCEP has been incorporated into the CFSv2.0 (Saha

100 et al., 2014) as a new model component. The latitude range of WW3 is 78°S–78°N with a spatial

101 resolution of 1/3°; the frequency range is 0.04118-0.4056Hz and the total number of frequencies is 25;

102 the number of wave directions is 24 with a resolution of 15°; the maximum global time step and the

103 minimum source term time step are both 180 s.

104 The   CFSv2.0   contains   two   components,   the   GFS   (details   are   available   at

105 http://www.emc.ncep.noaa.gov/GFS/doc.php) as the atmosphere component and the Modular Ocean

106 Model version 4 (MOM4; Griffies et al., 2004) as the ocean component. The MOM4 is integrated on a

107 nominal 0.5° horizontal grid with the enhanced horizontal resolution to 0.25° in the tropics, and has 40

108 vertical levels; the vertical spacing is 10 m in the upper 225 m, and then increases in unequal intervals to

109 the bottom at 4478.5 m. A three-layer sea ice model is included in MOM4 (Wu et al. 2005). The GFS

110 uses a spectral triangular truncation of 382 waves (T382) in the horizontal, which is equivalent to a grid

111 resolution of nearly 35 km, and 64 sigma-pressure hybrid layers in the vertical. The time steps of both

112 MOM4 and GFS are 180 s. The ocean and atmosphere components are then coupled at the same rate. In

113 the original two-way coupled system, the GFS receives SST from MOM4 and sends fluxes of heat,

114 momentum, freshwater to MOM4 (black arrows in Fig. 1).

115 The Chinese Community Coupler version 2.0 (C-Coupler2; Liu et al., 2018) is appliedused to

116 interpolate and pass variables between atmosphere and wave components as well as ocean and wave

117 components. Each component receives inputs and supplies outputs on its own grids. The C-Coupler2 is

118 a common, flexible and user-friendly coupler, which contains a dynamic 3-D coupling system and

119 enables variables to remain conserved after interpolation.

120 A schematic diagram of the coupled atmosphere-ocean-wave system is shown in Fig. 1. As illustrated,

121   WW3 is two-way coupled with MOM4 and GFS, through the C-Coupler2. WW3 is forced by 10-m wind

122   from GFS (green arrows) and surface current from MOM4 (blue arrows), and then generates and evolves

123   the wave action density spectrum. Meanwhile, the surface Stokes drift velocity, the Stokes transport and

124   the turbulent Langmuir number are passed to MOM4 (red arrows; see Section 2.3) from WW3, and the

125   surface Stokes drift velocity and the Charnock parameter are passed to GFS (red arrows; see Section 2.4

126   and 2.5). The high frequency tail assumption for Stokes drift in WW3 is used with a spectral level

127   decaying as f^{-5} (frequency). Additionally, the regular ocean surface current velocities from MOM4 are

128   also passed to GFS, to calculate the relative wind velocity for the turbulent fluxes together with surface

129   Stokes drift (blue arrows; see Section 2.4).

130   Both the CFSv2.0 and WW3 use warm starts; the initial fields at 00:00 UTC of the first day in each

131   experiment for CFSv2.0 were generated by the real time operational Climate Data Assimilation System

132   (Kalnay   et   al.,   1996),   downloaded   from   the   CFSv2.0   official   website

133   (http://nomads.ncep.noaa.gov/pub/data/nccf/com/cfs/prod). To get initial conditions for WW3, a stand-

134   alone WW3 model is set up synchronously (see Section 2.2). Since the interactions between waves and

135   sea ice are complicated and beyond the scope of the study, we turn off the coupling between WW3 and

136   CFSv2.0 in areas with sea ice.

137   In addition, to properly select the coupling frequency between CFSv2.0 and WW3, the root mean

138   square errors (RMSEs) of SST, significant wave height (SWH) and 10-m wind speed (WSP10) with

139   different coupling steps for the fully coupled experiment (ALL; details in Section 2.6) are calculated and

140   compared (Table S1 of the ~~supplementary~~supplementary material). The three components are coupled

141   every time step (180 s) in 1_STEP_ALL experiment, every 5 steps (900 s) in 5_STEP_ALL experiment

142   and every 10 steps (1800 s) in 10_STEP_ALL experiment. In 10_STEP_WW3, only the WW3 is coupled

143   every 10 time steps, whereas the GFS and the MOM4 remain the one time step (180 s) coupling frequency

144   as the original settings in CFSv2.0. From Table S1, the 10_STEP_WW3 experiment has a relatively short

145   runtime and small RMSEs. Therefore, the time steps of the 10_STEP_WW3 are selected to compromise

146   computing time consumption and model RMSEs.

147   **2.2 Initialization of WAVEWATCH III**

148   In WW3, input of momentum and energy by wind, and dissipation for wave-ocean interaction are two

149   important terms (combined as input-dissipation source term) in the energy balance equation

150   (WAVEWATCH III Development Group, 2016), which include the estimation of the Charnock

151   parameter related estimation. Several different packages to calculate the input-dissipation source term

152   (ST) are available offered in the WW3 version 5.16, including ST2 (Tolman and Chalikov, 1996), ST3

153   (Janssen, 2004; Bidlot, 2012), ST4 (Ardhuin et al., 2010), and ST6 (Zieger et al., 2015).

154   The initial wave fields were generated from 10-day simulation starting from rest in a stand-alone WW3

155   model. To minimize the biases of initial wave fields, we tested simulations with ST2, ST3, ST4, and ST6

156   schemes respectively, and compared the results with Janson-3 observations. Two 10-m wind datasets,

157   the Cross-Calibrated Multi-Platform (CCMP; Atlas et al., 2011) data and the fifth generation European

158   Centre for Medium-Range Weather Forecasts (ECMWF) Reanalysis (ERA5; Hersbach et al., 2020) data,

159   were used to drive the wave model respectively. Comparinged all results, the ST4 scheme with ERA5

160   wind forcing generates the minimum SWH bias (Table S2 in the supplementarysupplementary material),

161   consistent with findings in Stopa et al. (2016). Thus, the ST4 scheme was chosen to calculate the input

162   and dissipation term, and generate initial wave fields with ERA5 wind forcing for experiments listed in

163   Table 1. The parameters used for ST4 scheme followed TEST471f from WAVEWATCH III

164   Development Group (2016), which is the CFSR (CFS Reanalysis) tuned setup and is commonly-used at

165   global scale.

166   **2.3 Parameterizations of Stokes Drift-Related Ocean Mixing**

167   The full Stokes drift profile used in MOM4 is obtained by the method of Couvelard et al. (2020),

168   which is based on the work of Breivik et al. (2014; 2016). Breivik et al. (2016) derived the full Stokes

169   drift profile as

$$u_s B16(z) = u_s(0)[\exp(2k_p z) - \sqrt{-2\pi k_p z}\, \mathrm{erfc}(\sqrt{-2k_p z})], \qquad (1)$$

170   where~~The~~ $u_s(0)$ is the surface Stokes drift velocity, $k_p = \frac{u_s(0)}{6V_s}$, V_s is the Stokes transport, and erfc

171   is the complementary error function. Eqn. 1 is depth-averaged within each vertical grid interval as

$$u_s(z) = \frac{u_s(0)}{(th)_k}[I(z_{k+1/2}, k_p) - I(z_{k-1/2}, k_p)], \qquad (2)$$

$$I(z, k_p) = \frac{1}{6k_p}[e^{2k_p z} + 4k_p z \frac{u_s B16(z)}{u_s(0)}], \qquad (3)$$

172   where *th* is the thickness of layer *k*, following Li et al., (2017), Wu et al., (2019) and Couvelard et al.,

173   (2020).

174   **2.3.1 Mixing of Langmuir Turbulence**

175   McWilliams and Sullivan (2000) modified the turbulent velocity scale *W* in K-Profile Parameterization

176   (KPP) for vertical mixing by introducing an enhancement factor ε, to account for both boundary layer

177   depth changes and nonlocal mixing by Langmuir turbulence. Based on their work, Van Roekel et al.

178   (2012) improved the enhancement factor corresponding to alignment and misalignment of winds and

179   waves. Li et al. (2016) evaluated these parameterizations in a coupled global climate model, and found

180   that the difference between parameterizations with alignment and with misalignment was not significant,

181   owing to the relatively coarse resolution which cannot accurately represent the refraction by coasts and

182   current features. We ~~applied~~used the parameterization from Van Roekel et al. (2012) as well. Because

183   the resolution in our model is relatively coarse too, and the angles between winds and waves are less than

184   30° in most areas (Fig. S1i&j in the supplementary materials~~supplementary~~), we didn't consider

185   misalignment in the study.

186   W ($W=ku_*/\phi$, where u_* is the surface friction velocity, ϕ is the dimensionless flux profile, and

187   k=0.4 is the von Kármán constant) depends on~~varies in proportion to~~ the turbulent Langmuir number,

188   that is,

$$W = \frac{ku_*}{\phi}\varepsilon, \tag{4}$$

$$\varepsilon = \sqrt{1 + (3.1La_t)^{-2} + (5.4La_t)^{-4}}, \tag{5}$$

189   where La_t is the turbulent Langmuir number, defined as

$$La_t = \sqrt{\frac{u_*}{|u_s(0)|}}, \tag{6}$$

190   with $u_s(0)$ ~~is~~ the surface Stokes drift velocity.

191   Furthermore, the enhanced W will influence the calculation of boundary layer depth. In KPP the

192   boundary layer depth is determined as the smallest depth at which the bulk Richardson number equals

193   the critical value $Ri_{cr} = 0.3$, that is,

$$Ri_b(h) = \frac{gh[\rho_r - \rho(h)]}{\rho_0[|u_r - u(h)|^2 + W^2]} = Ri_{cr}, \tag{7}$$

194   where g is acceleration of gravity, ρ is density, u is velocity, ρ_r is surface density, u_r is surface

195   velocity, ρ_0 is the ~~an~~ average value of the density and h is the boundary layer depth. Hence, when W

196   is enhanced, the boundary layer depth h is deepened accordingly.

197 **2.3.2 Stokes–Coriolis Force and Associated Entrainment**

198   Because the Stokes drift velocity is an increment superimposed on the original current velocity, the

199   Coriolis force and the Stoke drift together produce an additional so-called Stokes–Coriolis (SC) force

200   (Hasselmann 1970), that is,

$$SC\ Force = \overrightarrow{u_s(z)} \times f\vec{z}. \tag{8}$$

201   Here $\overrightarrow{u_s(z)}$ is the Stokes drift velocity vector, f is the Coriolis frequency, and $\vec{z}$ is the vertical unity

202   vector. For consistency, the Stokes drift velocity is also included in advection terms of tracers (~~e.g.~~e.g.,

203   temperature, salinity) and convergence terms (Law-Chune and Aouf, 2018; Couvelard et al., 2020). And

204   the free surface condition for barotropic mode is correspondingly modified to

$$\frac{\partial \eta}{\partial t} = -\nabla M_{curr} - \nabla M_{st}, \tag{9}$$

205   where η is surface elevation, M_{curr} and M_{st} are the total vertical integral of regular Eulerian current

206   and Stokes drift, respectively.

207   To depict the entrainment below the ocean surface boundary layer induced by Stokes drift, Li et al.

208   (2016) suggested adding~~to add~~ the square of surface Stokes drift velocity ($|u_s(0)|^2$) to the denominator

209   of Eqn. 7, that is,

$$Ri_b(h) = \frac{gh[\rho_r - \rho(h)]}{\rho_0[|u_r - u(h)|^2 + W^2 + |u_s(0)|^2]} = Ri_{cr}. \tag{10}$$

210   The boundary layer depth h in KPP from Eqn. 10 is then enhanced due to Stokes drift velocity.

211   **2.4 Stokes Drift and Sea Surface Current on Air–Sea Fluxes**

212   At the air-sea boundary layer, the momentum flux (τ), sensible heat flux (SH) and freshwater flux (E)

213   are calculated as

$$\tau = \rho_a C_d |\Delta \vec{V}| \Delta \vec{V}, \qquad (11)$$

$$SH = \rho_a C_h |\Delta \vec{V}| \Delta \theta, \qquad (12)$$

$$E = \rho_a C_e |\Delta \vec{V}| \Delta q, \qquad (13)$$

214 where C_d, C_h, C_e are surface exchange coefficients for momentum, sensible heat and freshwater. ρ_a

215 is air density. $\Delta \theta, \Delta q$ are potential temperature and humidity differences between air and sea, and $\Delta \vec{V}$

216 is velocity of air relative to water flow.

217 In CFSv2.0, $\Delta \vec{V}$ is set to be wind speed ($\overrightarrow{U_{wind}}$). However, the effect of ocean surface current should

218 not be ignored. Luo et al. (2005) first indicated that including ocean surface current ($\overrightarrow{U_{surf}}$) improves

219 estimates of τ and subsequent ocean response. Renault et al. (2016) further indicated that the

220 improvements of τ by $\overrightarrow{U_{surf}}$ also feed back into atmosphere. At present, $\Delta \vec{V} = \overrightarrow{U_{wind}} - \overrightarrow{U_{surf}}$ is

221 widely used in coupled ocean-atmosphere models (e.g., Hersbach and Bidlot, 2008; Takatama et al.,

222 2017; Renault et al., 2021). Furthermore, Bao et al. (2019) indicated that as a part of the sea surface water

223 movement with speed magnitude comparable to surface current in mid-high latitudes, the surface Stokes

224 drift ($\overrightarrow{u_s(0)}$) should also be included, that is,

$$\Delta \vec{V} = \overrightarrow{U_{wind}} - \overrightarrow{U_{surf}} - \overrightarrow{u_s(0)}. \qquad (14)$$

225 To account for the effects of the surface currents and of the Stokes drift, Eqn. 14 was used~~To account for~~

226 ~~the effects of Stokes drift velocity, the Eqn. 14 was applied~~ in the coupled experiments (Table 1). To

227 complete the coupling, the corresponding modification of the tridiagonal matrix (Lemarié 2015) has been

228 implemented~~is also conducted~~ in CFSv2.0. Note that the direction of Stokes drift is generally consistent

229 with 10-m wind (Fig. S1i&j in ~~supplementary~~supplementary material), but the directions of surface

230 current and 10-m wind are usually different~~with an angle~~ due to Coriolis effect (Fig. S1g&h).

231 Consequently, the effects of $\overrightarrow{U_{surf}}$ and $\overrightarrow{u_s(0)}$ on $\Delta \vec{V}$ depend on the angles between them and $\overrightarrow{U_{wind}}$.

2.5 Parameterizations of Momentum Roughness

In CFSv2.0, the fluxes of momentum, heat, and freshwater are passed from atmosphere to ocean, and the estimates of them are critically important. The fluxes are in part determined by surface roughness length, which can be converted to surface exchange coefficients in Eqn. 11-13based on the Monin-Obukhov similarity theory (Monin and Obukhov, 1954).

2.5.1 The Momentum Roughness Length in GFS

In GFS, the momentum roughness length z_0 has two terms. The first term z_{ch} is parameterized by the Charnock relationship (Charnock, 1955) representing wave-resulted sea surface roughness, and the second term z_{vis} is the viscous contribution (Beljaars, 1994) for low winds and smooth surface, that is,

$$z_0 = z_{ch} + z_{vis} = \frac{C_{ch}u_*^2}{g} + \frac{0.11\nu}{u_*}. \qquad (15)$$

Here $C_{ch} = 0.014$ is the constant Charnock parameter, ν is the air kinematic viscosity. The relation of z_0 in GFS versus 10-m wind speed is shown in Fig.2 (black line).

2.5.2 The Charnock Relationship Related to Wave State

When ocean surface waves are explicitly considered, the Charnock parameter C_{ch} is not a constant (Janssen 1989, 1991; Taylor and Yelland, 2001; Moon et al., 2004; Drennan et al., 2003, 2005). In the study, we adopted a method developed by Moon et al. (2004), which considered the surface roughness leveling off under extremely high wind speed (Powell et al., 2003; Donelan et al., 2004). Based on observations, Moon et al. (2004) proposed Eqn. 16 to estimate the Charnock parameter by the wave age $\frac{c_{pi}}{u_*}$ (c_{pi} is the peak phase speed of the dominant wind-forced waves) with constant values of a and b changing with 10-m wind speed every 5 m/s in the range of 10 m/s to 50 m/s.

$$C_{ch} = a(\frac{c_{pi}}{u_*})^b,\qquad\qquad(16)$$

251 To obtain continuous values of a and b, we derive a new relationship (Eqn. 17) to estimate a and b from

252 10-m wind speed U_{10} by fitting the values in Table 1 of Moon et al. (2004),

$$a = \frac{1}{0.1477U_{10}{}^2 - 0.7395U_{10} - 10.9995},$$

$$(17)$$

$$b = 1.5661E^{-5}U_{10}{}^3 - 0.002U_{10}{}^2 + 0.1017U_{10} - 1.6182.$$

253 Because the observations in Moon et al. (2004) were obtained under tropical cyclones, Eqn. 17 is used

254 for U_{10}>15 m/s, whereas the original Charnock relationship of WW3 ST4 scheme (Janssen 1989, 1991)

255 is used for $U_{10} \leq 15$ m/s. The revised parameterization is called ST4-M04. Figure S2 in

256 ~~supplementary~~supplementary material shows the C_{ch} distribution obtained by Eqn. 16-17. In general

257 small wind direction variations at low latitudes lead to large wave age and thus low C_{ch}. The situation is

258 opposite at mid-high latitudes.

259  The relationships between z_0 and U_{10} in GFS, WW3 ST4 scheme (Janssen 1989, 1991) and ST4-

260 M04 scheme were compared in Fig.2. The z_0 in GFS increases relatively slowly with increasing wind

261 speed (black). The value of z_0 from ST4 scheme (purple) increases rapidly with wind speed at high

262 winds. In comparison, in ST4-M04 scheme (blue) the rapid increase of z_0 at high wind speed is

263 obviously restrained, although the mean z_0 is slightly higher than that in GFS at wind speed >10 m/s

264 due to larger C_{ch} (>0.014 in Fig. S2). Furthermore, since the Charnock number is constant in GFS, the

265 standard deviation (STD) of z_0 at a given wind speed is near zero. Since the z_0 is determined only by

266 wind-sea conditions in ST4 and ST4-M04 scheme, the STD at a given wind speed is mainly owing to

267 variations in wind fetch and development stage of sea state. The reduced STDs in ST4-M04 scheme,

268 compared to ST4, imply less sensitivity of z_0 to fetch and sea state. Note that the ST4-M04 is used in

269   GFS, while the z_0 in WW3 is still calculated by the ST4 source term to avoid affecting the balance of

270   adjusted wind input and dissipation.

271   **2.6 Set of Experiments**

272   A series of numerical experiments was conducted to evaluate the effects of aforementioned wave-

273   related processes on ocean and atmosphere in two 56-day periods, from January 3 to February 28, 2017

274   and from August 3 to September 28, 2018 for boreal winter and boreal summer, respectively.

275   The reference experiment (CTRL) is a one-way coupled experiment, in which CFSv2.0 provides 10-

276   m wind and surface current to WW3, whereas no variable is transferred from WW3 to CFSv2.0. The

277   results of CFSv2.0 in CTRL are consistent with the corresponding CFS Reanalysis data (Saha et al.,

278   2010). For each period, four sensitivity experiments were carried out (Table 1). Based on CTRL, the first

279   is the VR12-AL-SC-EN experiment, in which the Langmuir mixing parameterization is ~~applied~~used with

280   Stokes–Coriolis force and entrainment in MOM4. The second is the Z0-M04 experiment, in which the

281   constant C_{ch} in GFS is replaced by C_{ch} from WW3 ST4-M04 scheme. The effect of fluxes in GFS

282   generated by $\Delta\vec{V}$ (Eqn. 14) is tested in the FLUX experiment. The last experiment is the ALL, which

283   includes all three parameterizations.

284   **3 Data**

285   Due to the availability of in situ and reanalysis data in the simulation periods, only sea surface

286   temperature (SST), ocean subsurface temperature and salinity (T/S), 2-m air temperature (T02), 10-m

287   wind speed (WSP10), and significant wave height (SWH) were used to evaluate the simulation results.

288   The daily average satellite Optimum Interpolation SST (OISST) data were obtained from NOAA, with

289 0.25°×0.25° resolution (Reynolds et al., 2007; https://www.ncdc.noaa.gov/oisst). The global Argo

290 observational profiles of T/S (Li et al., 2019) were from China Argo Real-time Data Center

291 (www.argo.org.cn). The ERA5 datasets of T02, WSP10 and SWH with a spatial resolution of 0.5° were

292 also used (Hersbach et al., 2020; https://cds.climate.copernicus.eu/cdsapp#!/dataset/reanalysis-era5-

293 single-levels), which assimilated huge amounts of historical data and thus provided reliable hourly

294 estimates. Additionally, the WSP10 and SWH observations from the available National Data Buoy

295 Center (NDBC) buoy data (https://www.ndbc.noaa.gov) were used ~~applied~~ for comparison.

296 **4 Experimental Results**

297   In this section, an evaluation of simulation results was presented. Comparisons were made between

298 model results and observations/reanalysis data. The results in the first three days were excluded in the

299 evaluation, since the wave influences were weak at the beginning~~The results in the first three days were~~

300 ~~excluded in the evaluation, since the initial wave influences were too weak~~. Compared with observations

301 or ERA5, the general increase of the biases in all experiments is likely a drift from the initial conditions

302 since no data are assimilated.~~-~~

303 **4.1 Sea Surface Temperature (SST) and 2-m Air Temperature (T02)**

304   Figure 3a shows the spatial distribution of 53-day (day 4 to day 56) averaged SST biases in CTRL in

305 boreal winter, defined as SST in CTRL minus OISST. The global mean SST bias is approximately 0.32℃,

306 and the average RMSE is about 1.09℃ from day 4 to day 56 in CTRL (Fig. 3a). The simulated SSTs are

307 generally overestimated, and the large biases (>1.0℃) are mainly distributed in the Southern Ocean. In

308 Fig. 3b, the global-averaged RMSEs of CTRL (black) increase with time in the first month and then

309   gradually level off. Compared with CTRL, the RMSEs are reduced continuously in VR12-AL-SC-EN

310   and ALL (yellow and red), but not in Z0-M04 and FLUX (purple and blue).

311   To understand the critical ~~key~~ process responsible for the bias reduction in ALL, the SST differences

312   are compared across all four experiments (Fig.3c-f). Clearly, the difference in experiment VR12-AL-SC-

313   EN is similar to that in ALL (Fig. 3c&3f). The spatial correlation coefficient between the SST differences

314   with CTRL ~~OISST~~ of the two experiments (Fig. 3c&3f) is 0.67, significant at 99% confidence level, and

315   the RMSEs of SST are not different significantly (red and yellow lines in Fig. 3b), indicating the Stokes

316   drift-related parameterizations in VR12-AL-SC-EN mainly contribute to the SST positive bias reduction.

317   This contrasts with~~This is different with~~ Couvelard et al. (2020), where SST overestimations and MLD

318   underestimations are reduced mainly due to the directly modified turbulence kinetic energy scheme. The

319   global mean SST bias in ALL is 0.02 ℃ with RMSE of 1.03℃, and in most areas the SST differences

320   compared with CTRL are significant (P ≤0.05) (dotted areas in Fig. 3f). Large SST improvements

321   mainly appear in the Southern Ocean, with a regional RMSE decrease~~s~~ from 1.27 to 1.04 ℃ south of

322   45°S (Fig. 3f and red line in Fig. 5a). The reduction of overestimated SSTs in CTRL (red in Fig 3a) is

323   because the Stokes drift-related parameterizations in MOM4 inject turbulent kinetic energy into the

324   ocean, which enhance vertical mixing, and subsequently cool the surface waters (Belcher et al., 2012; Li

325   et al. 2016). The modified roughness and relative velocity in Z0-M04 and FLUX also influence upper

326   ocean mixing (Fig. 3d&e) via changing momentum flux, and lead to generally warmer SSTs (purple and

327   blue lines in Fig. 3b&5a). The effect from Stokes drift-related ocean mixing parameterizations dominates

328   SST changes in ALL.

329   In boreal summer, the global mean SST bias in CTRL is overestimated approximately 0.29℃, and the

330   averaged RMSE from day 4 to day 56 is about 1.19℃. The overestimated SSTs (>1.0℃) mainly occur

331   in the Northern Hemisphere (Fig. 4a). The global-averaged RMSEs are also generally lower in VR12-

332   AL-SC-EN and ALL than in CTRL (Fig. 4b). The cooling effects in VR12-AL-SC-EN lead to a global

333   mean bias of 0.06℃, and the large SST improvements mainly occur north of 50°N (Fig. 4c and yellow

334   line in Fig. 5b). The changes of SST in Z0-M04 and FLUX (Fig. 4d&e; purple and blue lines in Fig.

335   4b&5b) are relatively small. The global mean bias in ALL is 0.04℃ with an RMSE of 1.14℃ (Fig. 4f).

336   As aforementioned, large improvements of overestimated SST mainly occur at mid-high latitudes in

337   local summer. The time series of RMSEs and correlation coefficients of SST between model and

338   observation in the region (0-360°E, 45°-78°S in boreal winter and 0-360°E, 50°-78°N in boreal summer)

339   are shown in Fig. 5c-f. The RMSEs in CTRL (blue in Fig. 5c&d) increase in the first few weeks and then

340   gradually decrease afterward. Compared with CTRL, RMSEs in VR12-AL-SC-EN (yellow) and ALL

341   (red) are significantly (P≤0.01) reduced by about 0.3℃. The spatial correlation coefficients decrease

342   with time but remain high (>0.90) for all experiments (Fig. 5e&f) with higher values in experiment

343   VR12-AL-SC-EN (yellow).

344   We also compared T02 from experiments with ERA5 (Fig. 6). Warm biases of T02 appear in both

345   winter and summer in CTRL (Fig. 6a&b). The changes of T02 in sensitivity experiments (Fig. 6c-j) are

346   generally consistent with the changes of SST in the same experiments (Fig.3&4). The correlation

347   coefficients between the SST and the T02 changes for the ALL experiment in boreal winter and summer

348   (Fig. 3f&6f and Fig. 4f&6j) are 0.61 and 0.53 respectively, significant at 99% confidence level. In boreal

349   winter, all wave-coupled experiments except FLUX reduce the T02 mean bias (Fig.6c-f). VR12-AL-SC-

350   EC has the largest T02 bias reduction compared with CTRL, from 0.55℃ to 0.17℃ (Fig.6c). In boreal

351   summer, both VR12-AL-SC-EC and ALL have the largest T02 bias reduction, from 0.29℃ to 0.08℃

352   (Fig.6g&j). Noticeably, the improvements in RMSEs are not large for all experiments, because the

353   improvements mainly occur in areas with overestimated temperature.

4.2 Mixed Layer Depth (MLD)

355   To further evaluate the direct effect of the wave-related processes on the upper ocean, we compared

356   the MLD of all experiments with that estimated from Argo profiles in summer. The simulated T/S were

357   interpolated onto the positions of Argo profiles at the nearest time. The MLD was estimated as the depth

358   where the change of potential density reaches the value corresponding to a 0.2℃ decrease of potential

359   temperature with unchanged salinity from surface (de Boyer Montégut et al., 2004; Wang and Xu, 2018).

360   The time series of MLDs from numerical experiments and Argo south of 45°S in boreal winter (north

361   of 45°N in boreal summer) are compared in Fig. 7a (7b). The simulated MLDs are generally within the

362   STD of Argo MLDs (shading in Fig. 7). In CTRL, the mean bias (CTRL minus Argo) with STD is -

363   13.15±7.82 m (-6.75±5.29 m) in boreal winter (summer). The correlation coefficient of MLDs in CTRL

364   with Argo MLDs is 0.55 (0.68) with P ≤0.01, and the mean RMSE is 15.30 m (8.55 m) in boreal winter

365   (summer). In ALL, the mean bias (ALL minus Argo) with STD is 7.70±10.42 m (3.30±7.78 m) in boreal

366   winter (summer), and the correlation coefficient of MLDs enhances to 0.63 (0.78). The RMSE south of

367   45ºS decreases from 15.30 m in CTRL to 12.96 m in ALL. The RMSE north of 45ºN decreases from

368   6.71 m in CTRL to 5.55 m in ALL in the first six weeks but the value increases in the last two weeks due

369   to overestimation of MLDs. Compared with CTRL (orange in Fig. 7), VR12-AL-SC-EN (yellow) and

370   ALL (dark blue) show significantly improvements (P ≤0.01) on the underestimated MLDs time series,

371   whereas the MLDs difference between CTRL and Z0-M04 (purple)/FLUX (blue) is non-significant.

4.3 Wind Speed at 10 m (WSP10) and Significant Wave Height (SWH)

Compared with ERA5, the WSP10s in CTRL are generally overestimated in both winter and summer (Fig.8a&9a). The global averaged RMSEs of WSP10s in CTRL are 4.25 m/s (4.26 m/s) in boreal winter (summer). The global averaged RMSEs of WSP10s in all experiments increase with time in the first two weeks and then gradually level off with perturbations (Fig. 8b&9b). The differences of RMSEs between CTRL and other experiments are tiny in the first 10 days, and afterwards the RMSEs in Z0-M04 and ALL (purple and red) become clearly smaller than in CTRL over most of the time.

The comparisons of the simulated SWHs in CTRL with the ERA5 also show that the SWHs are overestimated in both winter and summer (Fig. 10a&11a). In boreal winter, the global mean SWH bias in CTRL is approximately 0.20 m with overestimates (> 0.30 m) in the Pacific, the North Atlantic and the Southern Ocean (Fig.10a), and the average RMSE is about 1.29 m. In boreal summer, the global mean bias in CTRL is approximately 0.17 m with 1.22 m RMSE (Fig. 11a). Similar to WSP10s, the RMSEs of SWHs also increase in the first two weeks and then gradually level off with perturbations (Fig. 10b&11b). The RMSEs in Z0-M04 and ALL (purple and red) are smaller than in CTRL over most of the time, consistent with changes of WSP10s. The correlation coefficients between changes of WSP10s and changes of SWHs in ALL are 0.77 and 0.73 in boreal winter and summer respectively (Fig. 8f&10f and Fig. 9f&11f), significant at 99% confidence level, indicating that the SWHs changes are closely related to changes of wind speeds.

In VR12-AL-SC-EN, the reduction of SST warm biases affects air temperature and stabilizes the marine atmospheric boundary layer (Sweet et al. 1981; O'Neill et al. 2003), and subsequently reduces WSP10s and SWHs with decreased global bias in boreal winter (Fig.8c&10c). In Z0-M04, the overestimated WSP10s and SWHs are also reduced (Fig. 8d&10d) due to the larger z_0 with the ST4-

394 M04 scheme at wind speed > 10 m/s (Fig. 2). The increase of z_0 enhances wind stress and momentum

395 transferred into the ocean, and therefore reduces surface winds (Pineau-Guillou et al. 2018; Sauvage et

396 al. 2020) and consequently reduces SWHs. In FLUX (Fig. 8e&10e), $\overrightarrow{U_{surf}}$ and $\overrightarrow{u_s(0)}$ decrease wind

397 stress and momentum transfer when their directions are consistent with wind directions, and vice versa

398 (Hersbach and Bidlot, 2008; Renault et al., 2016). For instance, the angles between wind and current are

399 relatively small (<90°) in the northeastern Pacific, reducing the wind stress and thus enhancing WSP10s

400 (Fig. 8e). In contrast, the large angles (>90°) between the northwesterlies and the Kuroshio in the

401 northwestern Pacific enhance wind stress, and decrease WSP10s (Fig. 8e). Consequently, the

402 improvements occur in areas with misalignment of winds and currents. With all combined effects, the

403 biases of WSP10s and SWHs in ALL in most regions are decreased (Fig. 8f&10f), with the reduced

404 global RMSEs of 4.17 m/s and 1.18 m respectively. In boreal summer, the improvements of WSP10s

405 and SWHs are relatively small in terms of global averaged RMSEs, because of smaller positive biases in

406 CTRL (Fig. 9a&11a). In ALL, the global averaged bias of WSP10s (SWHs) is -0.01 m/s (0.03 m). The

407 largest reduction primarily appears in the Southern Ocean (Fig. 9f&11f) to improve the overestimated

408 westerlies and SWHs in CTRL (Fig. 9a&11a).

409   Previous studies indicated that ocean surface winds in ERA5 are underestimated in some regions

410 (Belmonte Rivas and Stoffelen 2019; Kalverla et al. 2020; Sharmar and Markina 2020). To better

411 demonstrate the effects of waves on WSP10s and SWHs, comparisons of WSP10s and SWHs with the

412 NDBC buoy data are made (Table 2 and Fig. 12). The differences between sensitivity experiments and

413 CTRL are all statistically significant at 95% confidence level. Buoys are mainly located in the

414 northeastern Pacific, the tropical Pacific and the northwestern Atlantic oceans (Fig. S3), and buoy

415 identifiers with total numbers, longitudes and latitudes are listed in Table S3. The method from Hsu et al.

416 (1994) was used to adjust wind speeds from buoy data to the reference height of 10 m.

417   Compared to the NDBC data, the WSP10s and the SWHs in CTRL are generally overestimated in both

418 winter and summer with positive mean biases (Table 2 and Fig. 12). The reduction of mean biases appears

419 in all experiments except FLUX in boreal winter. The wave-related processes are most effective in areas

420 with positive biases, consistent with previous comparisons with ERA5. In boreal winter, the angles

421 between winds and currents are small. The wind stresses are then reduced in FLUX, and the WSP10s are

422 enhanced. So the positive bias is further enhanced. The improvements in ALL are generally the largest

423 (Table 2), with the WSP10s RMSE of 1.04 m/s (1.15 m/s) and the SWHs RMSE of 0.36 m (0.24 m) in

424 boreal winter (summer). As shown in Fig. 12, with the increase of WSP10s and SWHs, the reduction of

425 overestimation in ALL compared with CTRL is more prominent.

426 **5 Summary and Discussion**

427   To investigate the individual role played by wave-related processes on atmosphere and ocean interface

428 in a coupled global atmosphere-ocean-wave ~~modeling~~modelling system on intraseasonal scale, we

429 implemented the version 5.16 of WW3 into CFSv2.0 for global oceans from 78ºS-78ºN, using the C-

430 Coupler2. In this coupled system, the WW3 was forced by 10-m wind and surface current generated in

431 CFSv2.0. Stokes drift-related Langmuir mixing, Stokes-Coriolis force and entrainment in ocean, air-sea

432 fluxes modified by surface current and Stokes drift, and momentum roughness length (z_0) were

433 considered separately, and the results of sensitivity experiments were compared against in-situ buoys,

434 satellite measurements and ERA5 reanalysis. The effects of waves on intraseasonal prediction were

435 examined in two 56-day cases, one for boreal winter and the other one for boreal summer.

436   The following key results were found:

1. Overestimated SST, T02 and underestimated MLD in the mid-high latitudes in CFSv2.0 are significantly improved, particularly in local summer. Because enhanced vertical mixing generated by Langmuir turbulence, Stokes-Coriolis force and entrainment in VR12-AL-SC-EN changes temperature structure in the upper ocean, and further affects air temperature. In boreal winter, the regional RMSE of SST (T02) in the Southern Ocean decreases from 1.27 (1.93) in CTRL experiment to 1.04 (1.67) ℃ in ALL experiment. In boreal summer, the effect is weaker because of the smaller ocean areas in the mid-high latitudes of the Northern Hemisphere.

2. In general, all wave-related processes reduce~~lead to reduction of~~ biases for WSP10s and SWHs, particularly in regions where WSP10s and SWHs are overestimated. The decreased SSTs in VR12-AL-SC-EN stabilize the marine atmospheric boundary layer, and lead to weakened WSP10s and SWHs. The modified roughness in Z0-M04 generally enhances momentum transfer into the ocean, and so decreases WSP10s and SWHs. The relative wind-wave-current speed in FLUX also affects wind stress, and further influences WSP10s and SWHs. Compared with NDBC buoy observations and ERA5, the ALL experiment shows significant improvements.

In addition to the variables aforementioned, the changes of simulated enthalpy fluxes were also compared, which mainly depend on the WSP10s changes. However, the wave-related effects on enthalpy fluxes are non-significant for the 2-month simulation, so the results are not shown.

The wave-related parameterizations used in the study mainly improve model biases at mid-high latitudes, and SST biases in tropical oceans are only slightly improved (Fig. 3&4). Breivik et al. (2015) improved SST as well as subsurface temperature simulations in Nucleus for European Modelling of the

459   Ocean (NEMO) with parametrizations including the wave-related Charnock parameter, modification of

460   water-side stress with wind input and wave dissipation, wave dissipation-related turbulent kinetic energy

461   flux and the Stokes-Coriolis force. Based on a global NEMO-WW3 coupled framework, Couvelard et al.

462   (2020) modified the Charnock parameter, the Stokes drift-related forces and the Langmuir cell with

463   misalignment of winds and waves, the oceanic surface momentum flux and the turbulence kinetic energy

464   to reduce SST and MLD biases. In addition, sea sprays can enhance air-sea heat fluxes in the tropics

465   (Andreas et al. 2008; Andreas et al. 2015). We will consider more processes in the future studiesstudy.

466   Different parameterizations for the same wave-related process also deserve discussion. For ocean

467   surface roughness, the most classic parametrizations are those developed by Janssen (1989, 1991), Taylor

468   and Yelland (2001) and Drennan et al. (2003). The method of Taylor and Yelland (2001) requires the

469   peak wavelength for the total spectrum, whereas that of Drennan et al. (2003) only requires the peak of

470   wind-sea waves. This difference leads to the fact that the former is more suitable for a mixed sea state,

471   while the latter is more suitable for a young sea state (Drennan et al., 2005). And the effect of Janssen's

472   parameterization (1989, 1991) is similar to that of Drennan et al. (2003), since it is also based on the

473   wind-sea conditions (Shimura et al., 2017).

474   The case studies indicate that there remain significant biases in the coupled system, probably owing

475   to inaccuracy of coarse resolution, absence of a coupled wave-ice modular, and deficiency of initial fields.

476   In addition, to further improve the model and eliminate the biases, as Breivik et al. (2015) proposed,

477   extra adjusting of the individual model components in the coupled systems is also necessary. All of these

478   require further efforts to investigate efficient methods to improve fully coupled systems.

Code and data availability

The code developed for the coupled system can be found under https://doi.org/10.5281/zenodo.5811002

(Shi et al., 2021), including the coupling, preprocessing, run control and postprocessing scripts. The

initial fields for CFSv2.0 are generated by the real time operational Climate Data Assimilation System,

downloaded from the CFSv2.0 official website

(http://nomads.ncep.noaa.gov/pub/data/nccf/com/cfs/prod). The daily average satellite Optimum

Interpolation SST (OISST) data are obtained from NOAA (https://www.ncdc.noaa.gov/oisst), and the

National Data Buoy Center (NDBC) buoy data are also obtained from NOAA

(https://www.ndbc.noaa.gov). The Argo observational profiles of T/S are available at China Argo Real-

time Data Center (www.argo.org.cn). The ERA5 reanalysis are available at the Copernicus Climate

Change Service (C3S) Climate Date Store

(https://cds.climate.copernicus.eu/cdsapp#!/dataset/reanalysis-era5-single-levels).

Author contribution

FX and RS designed the experiments and RS carried them out. RS developed the code of coupling

parametrizations and produced the figures. ZF contributed to the installation and operation of CFSv2.0.

LL and HY contributed to the application of C-Coupler2. XL and YZ provided the original code of

CFSv2.0. RS prepared the manuscript with contributions from all co-authors. FX and HL contributed to

review and editing.

Acknowledgments

The authors would like to extend thanks to all developers of the CFSv2.0 model

(https://cfs.ncep.noaa.gov/cfsv2/downloads.html). The work was supported by National Key Research

and Development Program of China (no. 2016YFC1401408), and Tsinghua University Initiative

Scientific Research Program (2019Z07L01001). We thank Professor Wei Xue and Professor Yao Liu for

helping us test the coupling frequency. We also thank three anonymous reviewers and the handling editor

for their constructive comments~~We also thank two anonymous reviewers for their constructive comments~~.

References

Andreas, E. L., Mahrt, L., and Vickers, D.: An improved bulk air-sea surface flux algorithm, including

spray-mediated transfer, Quarterly Journal of the Royal Meteorological Society, 141, 642-654, 2015.

Andreas, E. L., Persson, P. O. G., and Hare, J. E.: A bulk turbulent air--sea flux algorithm for high-wind,

spray conditions, Journal of Physical Oceanography, 38, 1581-1596, 2008.

Ardhuin, F., Rogers, E., Babanin, A. V., Filipot, J., Magne, R., Roland, A., Der Westhuysen, A. V.,

Queffeulou, P., Lefevre, J. M., and Aouf, L.: Semiempirical Dissipation Source Functions for Ocean

Waves. Part I: Definition, Calibration, and Validation, Journal of Physical Oceanography, 40, 1917-1941,

http://dx.doi.org/10.1175/2010JPO4324.1, 2010.

Atlas, R., Hoffman, R. N., Ardizzone, J., Leidner, S. M., Jusem, J. C., Smith, D. K., and Gombos, D.: A

Cross-calibrated, Multiplatform Ocean Surface Wind Velocity Product for Meteorological and

Oceanographic Applications, Bulletin of the American Meteorological Society, 92, 157-174,

http://dx.doi.org/10.1175/2010BAMS2946.1, 2011.

Bao, Y., Song, Z., & Qiao, F.: FIO-ESM version 2.0: Model description and evaluation. Journal of

Geophysical Research: Oceans, 125, e2019JC016036. https://doi.org/10.1029/2019JC016036, 2019.

Belcher, S. E., Grant, A. L. M., Hanley, K., Foxkemper, B., Van Roekel, L., Sullivan, P. P., Large, W. G.,

Brown, A. R., Hines, A., and Calvert, D.: A global perspective on Langmuir turbulence in the ocean

521 surface boundary layer, Geophysical Research Letters, 39, http://dx.doi.org/10.1029/2012GL052932,

522 2012.

523 Beljaars, A. C. M.: The parametrization of surface fluxes in large-scale models under free convection. Q.

524 J. R. Meteorol. Soc., 121, 255{270. https://doi.org/10.1002/qj.49712152203, 1994.

525 Belmonte Rivas, M., and Stoffelen, A.: Characterizing ERA-Interim and ERA5 surface wind biases using

526 ASCAT, Ocean Science, 15, 831-852, 10.5194/os-15-831-2019, 2019.

527 Bidlot, J.-R., Prates, F., Ribas, R., et al.: Enhancing tropical cyclone wind forecasts, ECMWF newsletter,

528 164, 33-37. https://www.ecmwf.int/en/newsletter/164/meteorology/enhancing-tropical-cyclonewind-

529 forecasts, 2020.

530 Bidlot, J.-R.: Model upgrade improves ocean wave forecasts. ECMWF newsletter, 159, 10-10.

531 https://www.ecmwf.int/en/newsletter/159/news/modelupgrade-improves-ocean-wave-forecasts, 2019.

532 Bidlot, J.-R.: Present status of wave forecasting at ECMWF, Workshop on ocean waves, 25-27, 2012.

533 Breivik, Ø., Bidlot, J.-R., and Janssen, P. A.: A Stokes drift approximation based on the Phillips spectrum,

534 Ocean Modelling, 100, 49-56, 2016.

535 Breivik, Ø., Janssen, P. A., and Bidlot, J.-R.: Approximate Stokes drift profiles in deep water, Journal of

536 Physical Oceanography, 44, 2433-2445, 2014.

537 Breivik, Ø., Mogensen, K., Bidlot, J., Balmaseda, M., and Janssen, P. A. E. M.: Surface wave effects in

538 the NEMO ocean model: Forced and coupled experiments, Journal of Geophysical Research, 120, 2973-

539 2992, http://dx.doi.org/10.1002/2014JC010565, 2015.

540 Charnock, H.: Wind stress on a water surface, Quarterly Journal of the Royal Meteorological Society, 81,

541 639-640, http://dx.doi.org/10.1002/qj.49708135027, 1955.

Couvelard, X., Lemarié, F., Samson, G., Redelsperger, J.-L., Ardhuin, F., Benshila, R., and Madec, G.: Development of a two-way-coupled ocean-wave model: assessment on a global NEMO(v3.6)-WW3(v6.02) coupled configuration, Geosci. Model Dev., 13, 3067-3090, https://doi.org/10.5194/gmd-13-3067-2020, 2020.

de Boyer Montégut, C., Madec, G., Fischer, A. S., Lazar, A., and Iudicone, D.: Mixed layer depth over the global ocean: An examination of profile data and a profile‐based climatology, Journal of Geophysical Research, 109, http://dx.doi.org/10.1029/2004JC002378, 2004.

Donelan, M. A., Haus, B. K., Reul, N., Plant, W. J., Stiassnie, M., Graber, H. C., Brown, O. B., and Saltzman, E. S.: On the limiting aerodynamic roughness of the ocean in very strong winds, Geophysical Research Letters, 31, 10.1029/2004gl019460, 2004.

Drennan, W. M., H. C. Graber, D. Hauser, and C. Quentin: On the wave age dependence of wind stress over pure wind seas, J. Geophys. Res., 108(C3), 8062, doi:10.1029/2000JC000715, 2003.

Drennan, W. M., P. K. Taylor, and M. J. Yelland: Parameterizing the sea surface roughness, J. Phys. Oceanogr., 35(5), 835-848, 2005.

ECMWF: Official IFS Documentation CY47R1. In chap. PART VII: ECMWF wave model. Reading, UK: ECMWF, 10.21957/31drbygag, 2020.

Fan, Y., Lin, S., Held, I. M., Yu, Z., and Tolman, H. L.: Global Ocean Surface Wave Simulation Using a Coupled Atmosphere––Wave Model, Journal of Climate, 25, 6233-6252, http://dx.doi.org/10.1175/JCLI-D-11-00621.1, 2012.

Ghantous, M., and Babanin, A. V.: One-dimensional modelling of upper ocean mixing by turbulence due to wave orbital motion, Nonlinear Processes in Geophysics, 21, 325-338, 10.5194/npg-21-325-2014, 2014.

564   Griffies, S. M., Harrison, M. J., Pacanowski, R. C., and Rosati, A.: A technical guide to MOM4, GFDL

565   Ocean Group Tech. Rep, 5, 342, 2004.

566   Hasselmann, K.: Wave-driven inertial oscillations, Geophysical and Astrophysical Fluid Dynamics, 1,

567   463-502, http://dx.doi.org/10.1080/03091927009365783, 1970.

568   Hersbach H. and Bidlot, J.-R.: The relevance of ocean surface current in the ECMWF analysis and

569   forecast system. Proceeding from the ECMWF Workshop on Atmosphere-Ocean Interaction, 10-12,

570   https://www.ecmwf.int/sites/default/files/elibrary/2009/9866-relevance-ocean-surface-current-ecmwf-

571   analysis-and-forecast-system.pdf, 2008.

572   Hersbach, H., Bell, B., Berrisford, P., Hirahara, S., et al.: The ERA5 Global Reanalysis, Quarterly Journal

573   of the Royal Meteorological Society, Soc. 00: 363 (2020), https://doi.org/10.1002/qj.3803, 2020.

574   Hsu, S. A., Eric A. Meindl, and David B. Gilhousen: Determining the Power-Law Wind-Profile Exponent

575   under Near-Neutral Stability Conditions at Sea, Applied Meteorology, Vol. 33, No. 6,

576   https://doi.org/10.1175/1520-0450(1994)033<0757:DTPLWP>2.0.CO;2, 1994.

577   Janssen, P. A. E. M.: The interaction of ocean waves and wind, Cambridge University Press, pp 312,

578   2004.

579   Janssen, P. A. E. M.: The Quasi-linear theory of wind wave generation applied to wave forecasting. J.

580   Phys.   Oceanogr.   21,   1631-1642.   https://doi.org/10.1175/1520-

581   0485(1991)021<1631:QLTOWW>2.0.CO;2, 1991.

582   Janssen, P. A. E. M.: Wave-induced stress and the drag of air flow over sea waves. J. Phys. Oceanogr.

583   19(6), 745-754. https://doi.org/10.1175/1520-1310 0485(1989)019<0745:WISATD>2.0.CO;2, 1989.

584   Kalnay, E., Kanamitsu, M., Kistler, R., Collins, W. D., Deaven, D. G., Gandin, L. S., Iredell, M. D., Saha,

585   S., White, G. H., and Woollen, J.: The NCEP/NCAR 40-Year Reanalysis Project, Bulletin of the

586 American Meteorological Society, 77, 437-471, http://dx.doi.org/10.1175/1520-

587 0477(1996)077%3C0437:TNYRP%3E2.0.CO;2, 1996.

588 Kalverla, P. C., Holtslag, A. A. M., Ronda, R. J., and Steeneveld, G.-J.: Quality of wind characteristics

589 in recent wind atlases over the North Sea, Quarterly Journal of the Royal Meteorological Society, 146,

590 1498-1515, 10.1002/qj.3748, 2020.

591 Kukulka, T., Plueddemann, A. J., Trowbridge, J. H., and Sullivan, P. P.: Significance of Langmuir

592 circulation in upper ocean mixing: comparison of observations and simulations, Geophysical Research

593 Letters, 36, http://dx.doi.org/10.1029/2009GL037620, 2009.

594 Law-Chune, S., and Aouf, L.: Wave effects in global ocean modeling: parametrizations vs. forcing from

595 a wave model, Ocean Dynamics, 68, 1739-1758, http://dx.doi.org/10.1007/s10236-018-1220-2, 2018.

596 Lemarié, F.: Numerical modification of atmospheric models to include the feedback of oceanic currents

597 on air-sea fluxes in ocean-atmosphere coupled models, INRIA Grenoble-Rhône-Alpes, Laboratoire Jean

598 Kuntzmann, https://hal.inria.fr/hal-01184711/document, 2015.

599 Li, D., Staneva, J., Bidlot, J.-R., Grayek, S., Zhu, Y., and Yin, B.: Improving Regional Model Skills

600 During Typhoon Events: A Case Study for Super Typhoon Lingling Over the Northwest Pacific Ocean,

601 Frontiers in Marine Science, 8, 10.3389/fmars.2021.613913, 2021.

602 Li, M., and Garrett, C.: Mixed Layer Deepening Due to Langmuir Circulation, Journal of Physical

603 Oceanography, 27, 121-132, http://dx.doi.org/10.1175/1520-

604 0485(1997)027%3C0121:MLDDTL%3E2.0.CO;2, 1997.

605 Li, Q., Foxkemper, B., Breivik, O., and Webb, A.: Statistical models of global Langmuir mixing, Ocean

606 Modelling, 113, 95-114, http://dx.doi.org/10.1016/j.ocemod.2017.03.016, 2017.

607   Li, Q., Webb, A., Foxkemper, B., Craig, A., Danabasoglu, G., Large, W. G., and Vertenstein, M.:

608   Langmuir mixing effects on global climate: WAVEWATCH III in CESM, Ocean Modelling, 103, 145-

609   160, http://dx.doi.org/10.1016/j.ocemod.2015.07.020, 2016.

610   Li, Z., Liu, Z., & Xing, X.: User Manual for Global Argo Observational data set (V3.0) (1997-2019),

611   China Argo Real-time Data Center, Hangzhou, 37pp, 2019.

612   Liu, L., Zhang, C., Li, R., and Wang, B.: C-Coupler2: a flexible and user-friendly community coupler for

613   model coupling and nesting, Geoscientific Model Development Discussions, 11, 1-63,

614   http://dx.doi.org/10.5194/gmd-11-3557-2018, 2018.

615   Luo, J.J., Masson, S., Roeckner, E., Madec, G., & Yamagata, T.: Reducing climatology Bias in an ocean-

616   atmosphere CGCM with improved coupling physics. Journal of Climate, 18(13), 2344-2360.

617   https://doi.org/10.1175/JCLI3404.1, 2005.

618   Mcwilliams, J. C., and Sullivan, P. P.: Vertical Mixing by Langmuir Circulations, Spill Science &

619   Technology Bulletin, 6, 225-237, http://dx.doi.org/10.1016/S1353-2561(01)00041-X, 2000.

620   Monin, A. S., and Obukhov, A. M.: Basic laws of turbulent mixing in the surface layer of the atmosphere,

621   Contrib. Geophys. Inst. Acad. Sci. USSR, 151(163), e187, 1954.

622   Moon, I., Ginis, I., and Hara, T.: Effect of surface waves on Charnock coefficient under tropical cyclones,

623   Geophysical Research Letters, 31, http://dx.doi.org/10.1029/2004GL020988, 2004.

624   Moum J.N., and Smyth W.D.: Upper Ocean Mixing. In Cochran, J. Kirk; Bokuniewicz, J. Henry; Yager,

625   L. Patricia (Eds.) Encyclopedia of Ocean Sciences, 3rd Edition. vol. 1, pp. 71-79, Elsevier. ISBN: 978-

626   0-12-813081-0, 2019.

O'Neill, L. W., Chelton, D. B., and Esbensen, S. K.: Observations of SST-induced perturbations of the wind stress field over the Southern Ocean on seasonal timescales, Journal of Climate, 16, 2340-2354, 10.1175/2780.1, 2003.

Pineau-Guillou L., Ardhuin,F., Bouin,M.N.,Redelsperger,J.L.,Chapron,B., Bidlot, J. R., & Quilfen, Y.: Strong winds in a coupled wave-atmosphere model during a North Atlantic storm event: evaluation against observations. Quarterly Journal of the Royal Meteorological Society, 144(711), 317-332, 2018.

Polonichko, V.: Generation of Langmuir circulation for nonaligned wind stress and the Stokes drift, J. Geophys. Res., 102, 15773-- 15780, https://doi.org/10.1029/97JC00460, 1997.

Powell, M. D., Vickery, P. J., and Reinhold, T. A.: Reduced drag coefficient for high wind speeds in tropical cyclones, Nature, 422, 279-283, 10.1038/nature01481, 2003.

Qiao, F., Yuan, Y., Yang, Y., Zheng, Q., Xia, C., and Ma, J.: Wave‐induced mixing in the upper ocean: Distribution and application to a global ocean circulation model, Geophysical Research Letters, 31, http://dx.doi.org/10.1029/2004GL019824, 2004.

Renault, L., Arsouze, T., and Ballabrera-Poy, J.: On the Influence of the Current Feedback to the Atmosphere on the Western Mediterranean Sea Dynamics, Journal of Geophysical Research-Oceans, 126, 10.1029/2020jc016664, 2021.

Renault, L., Molemaker, M. J., McWilliams, J. C., Shchepetkin, A. F., Lemarie, F., Chelton, D., Illig, S., and Hall, A.: Modulation of Wind Work by Oceanic Current Interaction with the Atmosphere, Journal of Physical Oceanography, 46, 1685-1704, 10.1175/jpo-d-15-0232.1, 2016.

Reynolds, R. W., Smith, T. M., Liu, C., Chelton, D. B., Casey, K. S., and Schlax, M. G.: Daily High-Resolution-Blended Analyses for Sea Surface Temperature, Journal of Climate, 20, 5473-5496, http://dx.doi.org/10.1175/2007JCLI1824.1, 2007.

649   Saha, S., Moorthi, S., Pan, H., Wu, X., Wang, J., Nadiga, S., Tripp, P., Kistler, R., Woollen, J., and

650   Behringer, D.: The NCEP Climate Forecast System Reanalysis, Bulletin of the American Meteorological

651   Society, 91, 1015-1057, http://dx.doi.org/10.1175/2010BAMS3001.1, 2010.

652   Saha, S., Moorthi, S., Wu, X., Wang, J., Nadiga, S., Tripp, P., Behringer, D., Hou, Y., Chuang, H., and

653   Iredell, M. D.: The NCEP Climate Forecast System Version 2, Journal of Climate, 27, 2185-2208,

654   http://dx.doi.org/10.1175/JCLI-D-12-00823.1, 2014.

655   Sauvage, C., Lebeaupin Brossier, C., Bouin, M. N., & Ducrocq, V.: Characterization of the air-sea

656   exchange mechanisms during a Mediterranean heavy precipitation event using realistic sea state

657   modelling. Atmospheric Chemistry & Physics, 20(3), 2020.

658   Sharmar, V., and Markina, M.: Validation of global wind wave hindcasts using ERA5, MERRA2, ERA-

659   Interim and CFSRv2 reanalyzes, IOP Conference Series: Earth and Environmental Science, 606, 012056

660   (012059 pp.)-012056 (012059 pp.), 10.1088/1755-1315/606/1/012056, 2020.

661   Shimura, T., Mori, N., Takemi, T., et al.: Long term impacts of ocean wave-dependent roughness on

662   global climate systems. Journal of Geophysical Research: Oceans, 122(3),

663   https://doi.org/10.1002/2016JC012621, 2017.

664   Stopa, J. E., Ardhuin, F., Babanin, A. V., and Zieger, S.: Comparison and validation of physical wave

665   parameterizations in spectral wave models, Ocean Modelling, 103, 2-17,

666   http://dx.doi.org/10.1016/j.ocemod.2015.09.003, 2016.

667   Sweet, W., Fett, R., Kerling, J., and Laviolette, P.: Air—sea interaction effects in the lower troposphere

668   across the north wall of the Gulf Stream, Mon. Weather Rev., 109, 1042-1052, 10.1175/1520-

669   0493(1981)109<1042:Asieit>2.0.Co;2, 1981.

670 Takatama, K., and Schneider, N.: The Role of Back Pressure in the Atmospheric Response to Surface

671 Stress Induced by the Kuroshio, Journal of the Atmospheric Sciences, 74, 597-615, 10.1175/jas-d-16-

672 0149.1, 2017.

673 Taylor, P. K., and Yelland, M. J.: The Dependence of Sea Surface Roughness on the Height and Steepness

674 of the Waves, Journal of Physical Oceanography, 31, 572-590, http://dx.doi.org/10.1175/1520-

675 0485(2001)031%3C0572:TDOSSR%3E2.0.CO;2, 2001.

676 Terray, E. A., Donelan, M. A., Agrawal, Y. C., Drennan, W. M., Kahma, K. K., Williams, A. J., Hwang,

677 P. A., and Kitaigorodskii, S. A.: Estimates of Kinetic Energy Dissipation under Breaking Waves, Journal

678 of Physical Oceanography, 26, 792-807, http://dx.doi.org/10.1175/1520-

679 0485(1996)026%3C0792:EOKEDU%3E2.0.CO;2, 1996.

680 Tolman, H. L., and Chalikov, D. V.: Source Terms in a Third-Generation Wind Wave Model, Journal of

681 Physical Oceanography, 26, 2497-2518, http://dx.doi.org/10.1175/1520-

682 0485(1996)026%3C2497:STIATG%3E2.0.CO;2, 1996.

683 Van Roekel, L. P., Foxkemper, B., Sullivan, P. P., Hamlington, P. E., and Haney, S.: The form and

684 orientation of Langmuir cells for misaligned winds and waves, Journal of Geophysical Research, 117,

685 http://dx.doi.org/10.1029/2011JC007516, 2012.

686 Wang, L., and Xu, F.: Decadal variability and trends of oceanic barrier layers in tropical Pacific, Ocean

687 Dynamics, 68, 1155-1168, 10.1007/s10236-018-1191-3, 2018.

688 WAVEWATCH III Development Group.: User manual and system documentation of WAVEWATCH III

689 version 5.16, NOAA/NWS/NCEP/MMAB Technical Note 329, 326, 2016.

690 Wu, L., Staneva, J., Breivik, Ø., Rutgersson, A., Nurser, A. G., Clementi, E., and Madec, G.: Wave effects

691 on coastal upwelling and water level, Ocean Modelling, 140, 101405, 2019.

692   Wu, X., K. S. Moorthi, K. Okomoto, and H. L. Pan: Sea ice impacts on GFS forecasts at high latitudes,

693   Proceedings of the 85th AMS Annual Meeting, 8th Conference on Polar Meteorology and Oceanography,

694   San Diego, CA, 2005.

695   Zieger, S., Babanin, A. V., Rogers, W. E., and Young, I. R.: Observation-based source terms in the third-

696   generation   wave   model   WAVEWATCH,   Ocean   Modelling,   96,   2-25,

697   http://dx.doi.org/10.1016/j.ocemod.2015.07.014, 2015.

Table 1. List of numerical experiments: setups different from CTRL are marked with bold

Experiments	Physical Process/Parameterization		
	Langmuir Cell with Stokes-Coriolis Force and Entrainment	Roughness (Charnock Parameter)	Relative Velocity in Flux
CTRL	Off	Off	Off
VR12-AL-SC-EN	**Eqn. 1-6, 8-10**	Off	Off
Z0-M04	Off	$\mathbf{C_{ch}}$ **from Eqn. 16, 17**	Off
FLUX	Off	Off	$\mathbf{\Delta\vec{V}}$ **from Eqn. 14**
ALL	**Eqn. 1-6, 8-10**	$\mathbf{C_{ch}}$ **from Eqn. 16, 17**	$\mathbf{\Delta\vec{V}}$ **from Eqn. 14**

Table 2. The 53-day mean bias with standard deviation (STD) and RMSE for WSP10 and SWH compared with NDBC buoy observation: the bias is calculated as simulation minus NDBC.

Boreal Winter WSP10	Bias with STD	RMSE
CTRL	0.16±1.23	1.24
VR12-AL-SC-EN	0.01±1.12	1.12
Z0-M04	-0.01±1.07	1.07
FLUX	0.39±1.20	1.26
ALL	0.07±1.04	1.04
Boreal Winter SWH	**Bias with STD**	**RMSE**
CTRL	0.21±0.38	0.44
VR12-AL-SC-EN	0.14±0.35	0.37
Z0-M04	0.10±0.30	0.32
FLUX	0.24±0.34	0.42
ALL	0.12±0.34	0.36
Boreal Summer WSP10	**Bias with STD**	**RMSE**
CTRL	0.15±1.23	1.24
VR12-AL-SC-EN	-0.03±1.22	1.22
Z0-M04	-0.04±1.21	1.21
FLUX	-0.22±1.18	1.20
ALL	-0.17±1.14	1.15
Boreal Summer SWH	**Bias with STD**	**RMSE**
CTRL	0.28±0.25	0.38
VR12-AL-SC-EN	0.19±0.24	0.30
Z0-M04	0.22±0.26	0.34
FLUX	0.14±0.25	0.29
ALL	0.12±0.21	0.24
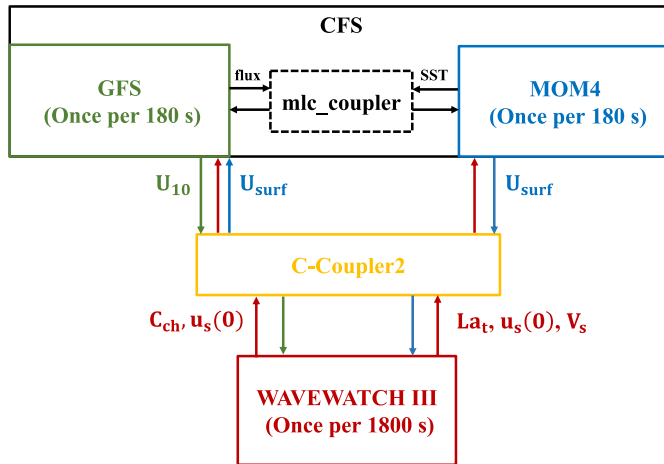
Figure 1. A schematic diagram of the atmosphere-ocean-wave coupled modeling system. The arrows indicate the coupled variables that are passed between the model components. In the diagram, C_{ch}, La_t, $u_s(0)$, V_s, U_{10}, and U_{surf} are Charnock parameter (red arrows), turbulent Langmuir number (red arrows), surface Stokes drift velocity (red arrows), Stokes transport (red arrows), 10-m wind (green arrows) and surface current (blue arrows), respectively.
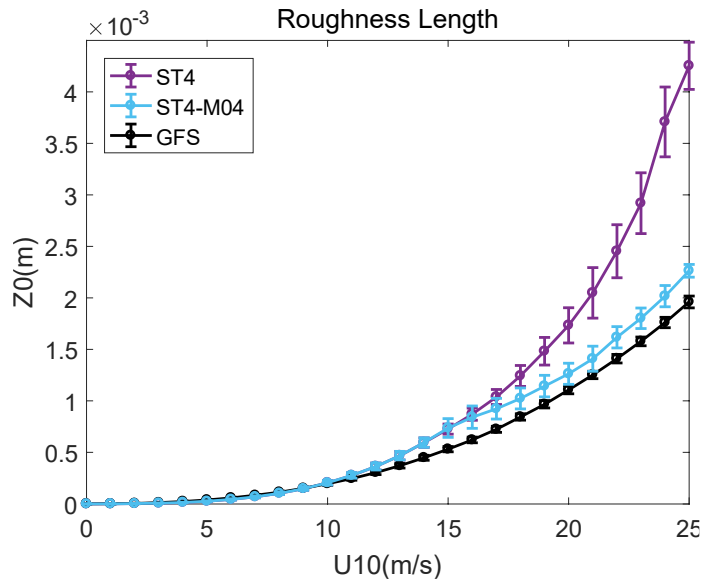
Figure 2. Relationships between momentum roughness length z_0 (m) in the coupled system and 10-m wind speed (m/s); error bars indicate twice the standard deviations for each point.
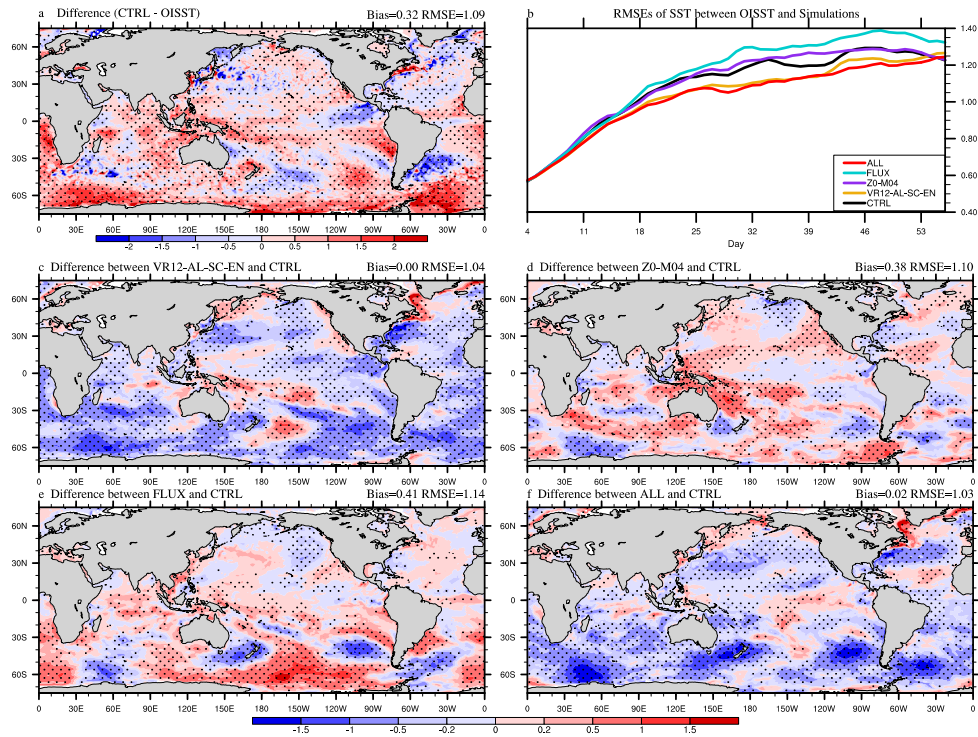
Figure 3. The 53-day average SST (℃) bias in CTRL (a; CTRL minus OISST), the time series of global-averaged RMSE (b), and the differences between VR12-AL-SC-EN (c)/Z0-M04 (d)/ FLUX (e)/ ALL (f) and CTRL in Jan-Feb, 2017 (VR12-AL-SC-EN/Z0-M04/FLUX/ALL minus CTRL). The first 3-day simulation is discarded. The dotted areas are statistically significant at 95% confidence level.
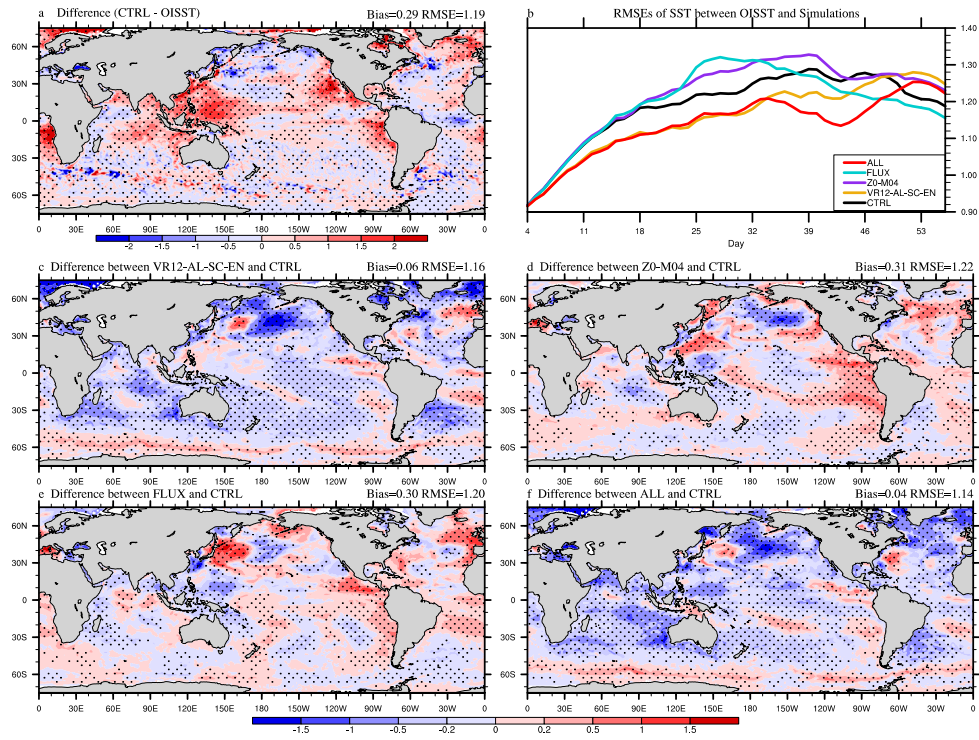
Figure 4. The same as Figure 3 but for Aug-Sep, 2018.
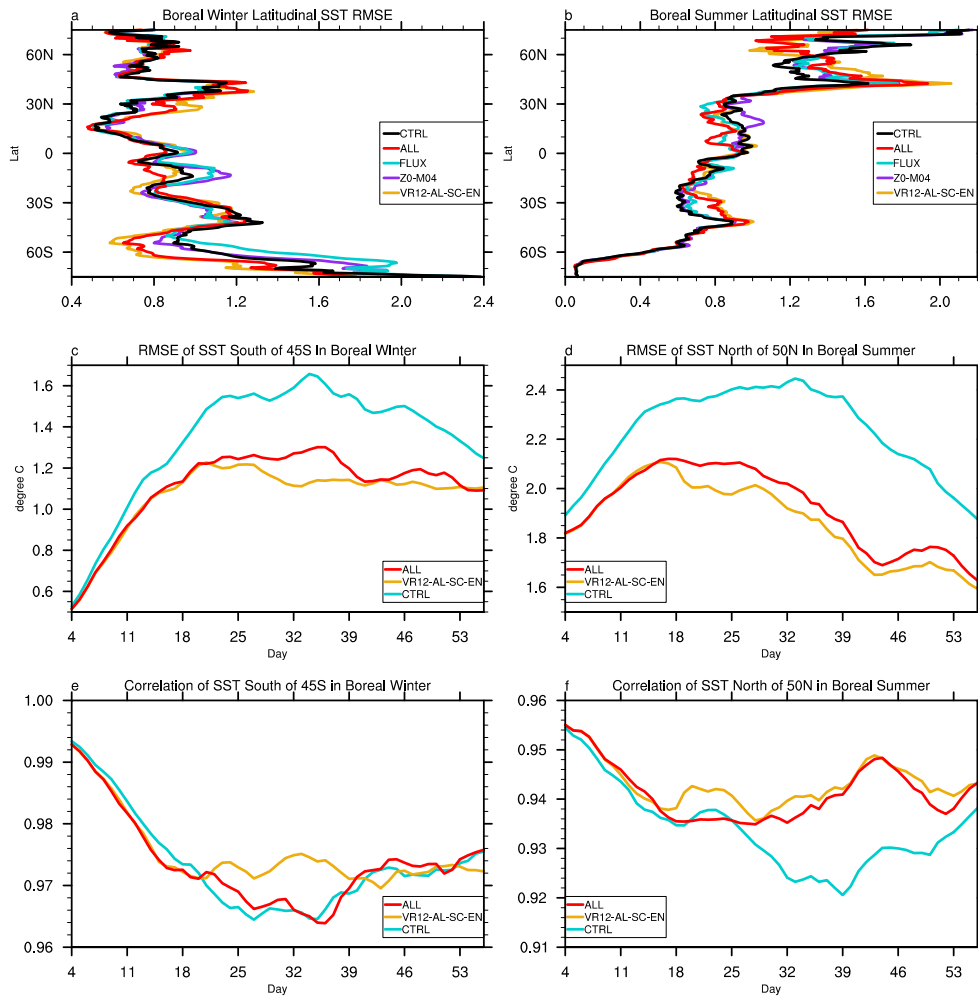
Figure 5. The 53-day averaged latitudinal distribution of SST root mean square errors (RMSE), time series of domain-averaged SST RMSE and correlation coefficient: **a/b** the latitudinal RMSE in boreal winter/summer compared with OISST, **c/d** the time series of domain-averaged (0-360°E, 45-78°S/50-78°N) SST RMSE in boreal winter/summer, **e/f** the time series of domain-averaged (0-360°E, 45-78°S/50-78°N) SST correlation coefficient in boreal winter/summer; differences of RMSE and correlation coefficient time series between VR12-AL-SC-EN/ALL and CTRL are statistically significant at 99% confidence level, except those in Fig. e.
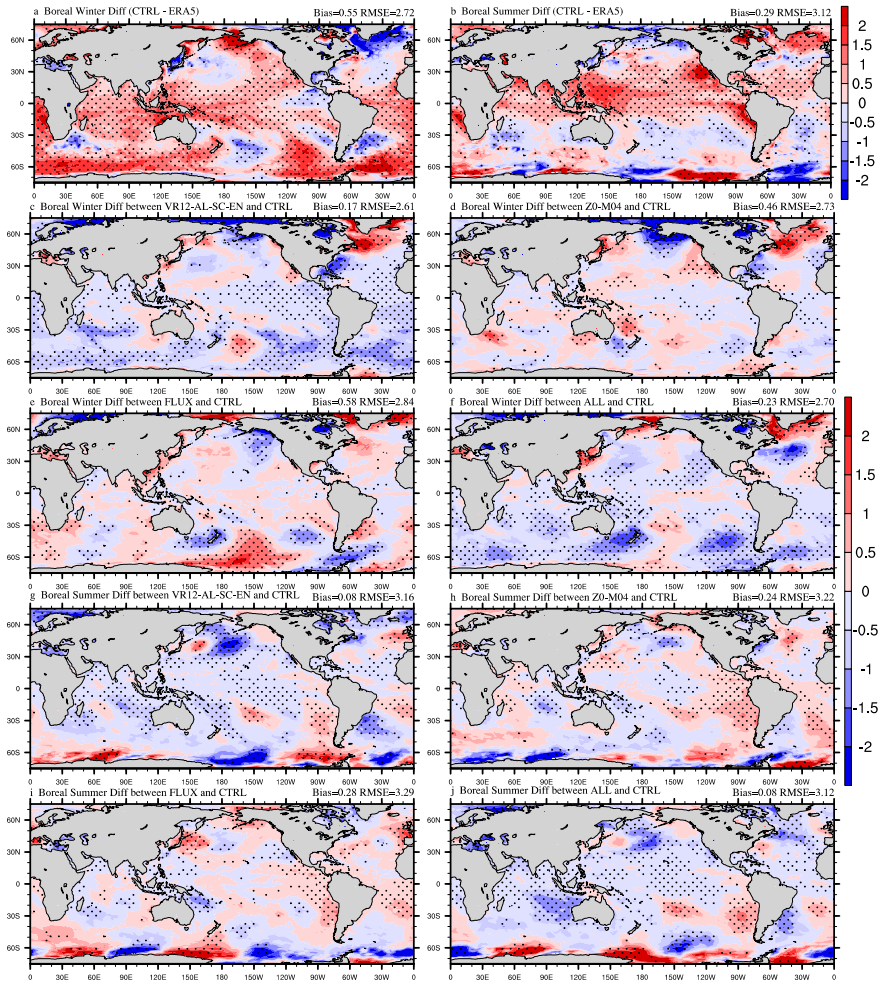
Figure 6. The 53-day average T02 (°C) bias in CTRL (a&b; CTRL minus ERA5), and the differences between VR12-AL-SC-EN (c&g)/Z0-M04 (d&h)/ FLUX (e&i)/ ALL (f&j) and CTRL (VR12-AL-SC-EN/Z0-M04/FLUX/ALL minus CTRL). The first 3-day simulation is discarded. The dotted areas are statistically significant at 95% confidence level. a/c/d/e/f are for Jan-Feb, 2017, and b/g/h/i/j are for Aug-Sep, 2018.
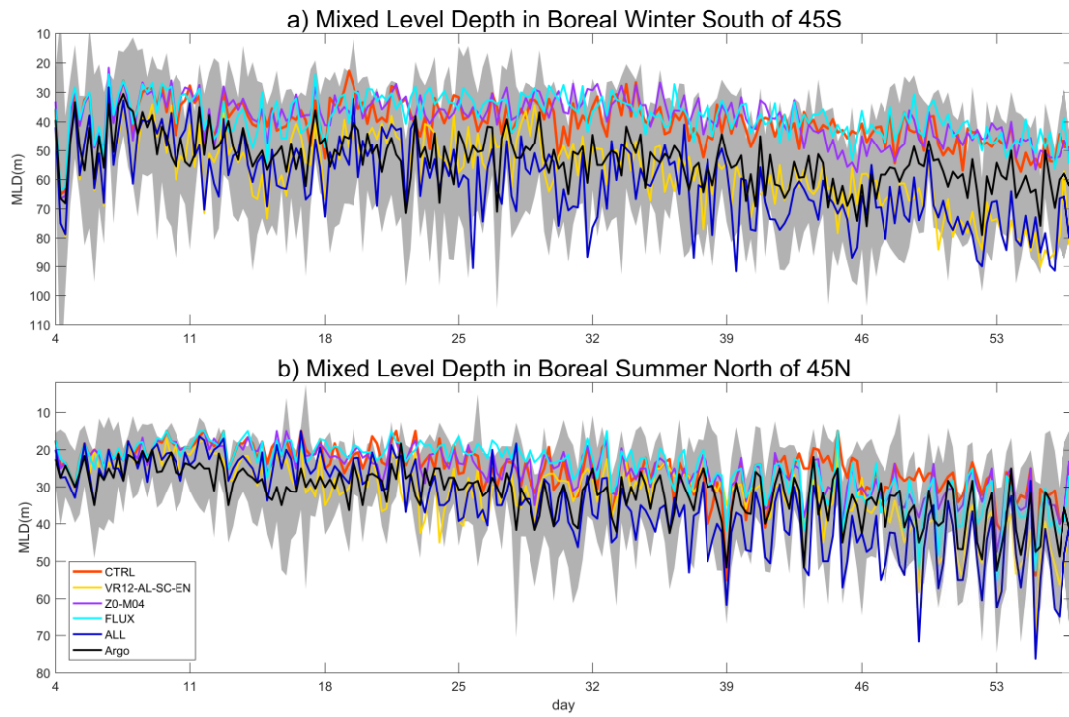
Figure 7. The 53-day time series of domain-averaged (0-360°E, 45-78°S/N) mixed layer depth (MLD; m) in boreal winter/summer: the difference between CTRL and VR12-AL-SC-EN/ALL passes the student's t-test at 99% confidence level; the time intervals are 6 hours; shaded areas indicate twice the standard deviations for Argo.
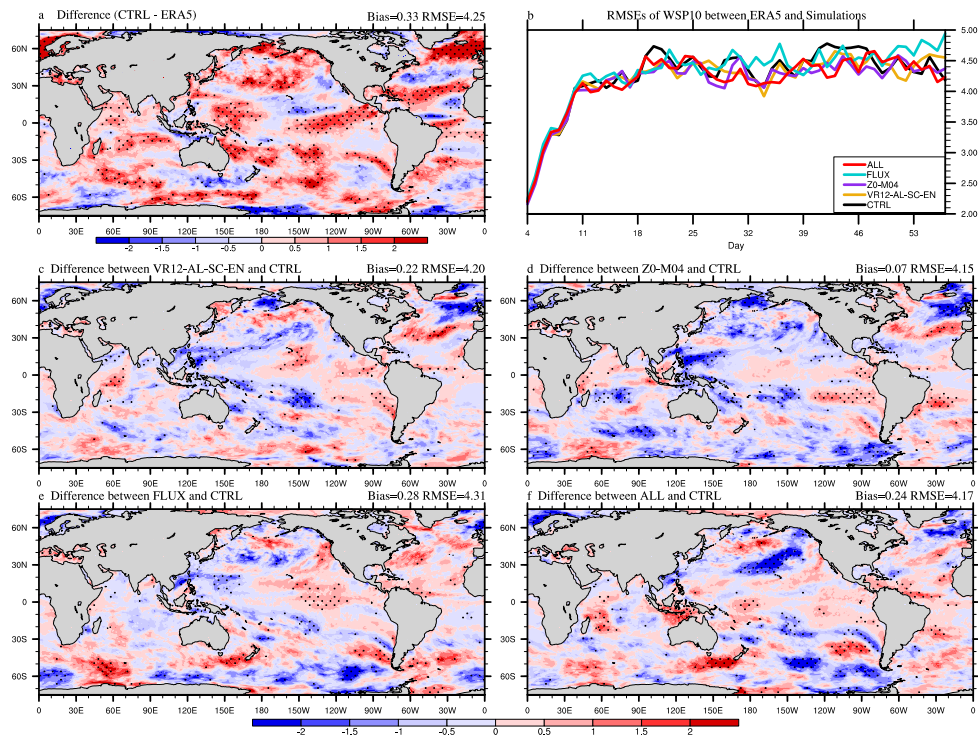
Figure 8. The 53-day average WSP10 (m/s) bias in CTRL (a; CTRL minus ERA5), the time series of global-averaged RMSE (b), and the differences between VR12-AL-SC-EN (c)/Z0-M04 (d)/ FLUX (e)/ ALL (f) and CTRL in Jan-Feb, 2017 (VR12-AL-SC-EN/Z0-M04/FLUX/ALL minus CTRL). The first 3-day simulation is discarded. The dotted areas are statistically significant at 95% confidence level.
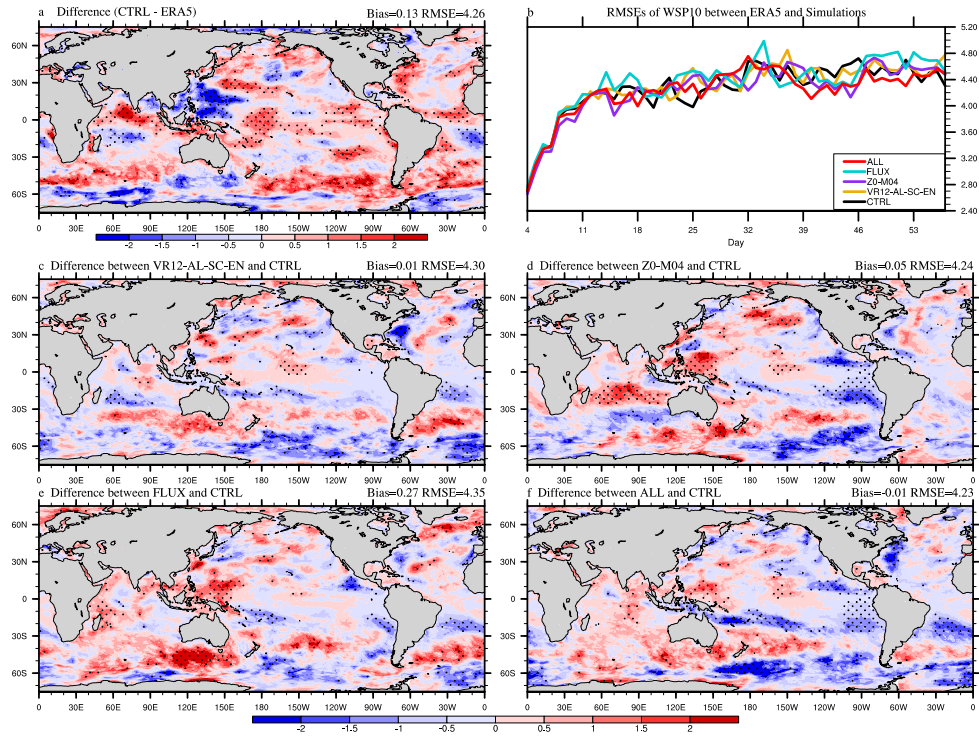
Figure 9. The same as Figure 8 but for Aug-Sep, 2018.
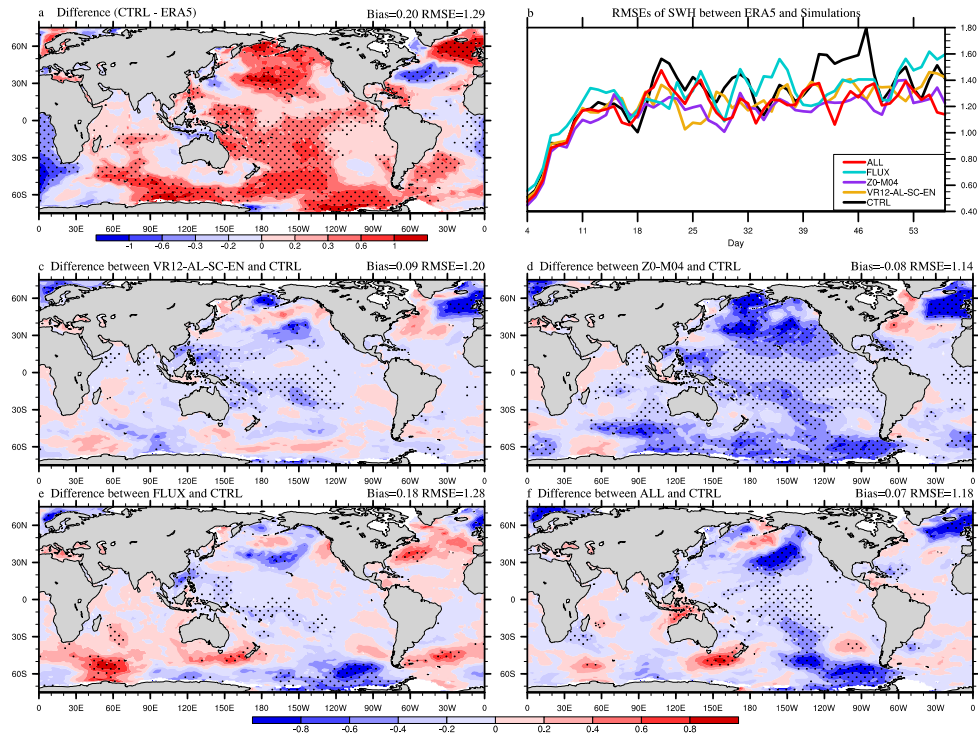
Figure 10. The 53-day average SWH (m) bias in CTRL (a; CTRL minus ERA5), the time series of global-averaged RMSE (b), and the differences between VR12-AL-SC-EN (c)/Z0-M04 (d)/ FLUX (e)/ ALL (f) and CTRL in Jan-Feb, 2017 (VR12-AL-SC-EN/Z0-M04/FLUX/ALL minus CTRL). The first 3-day simulation is discarded. The dotted areas are statistically significant at 95% confidence level.
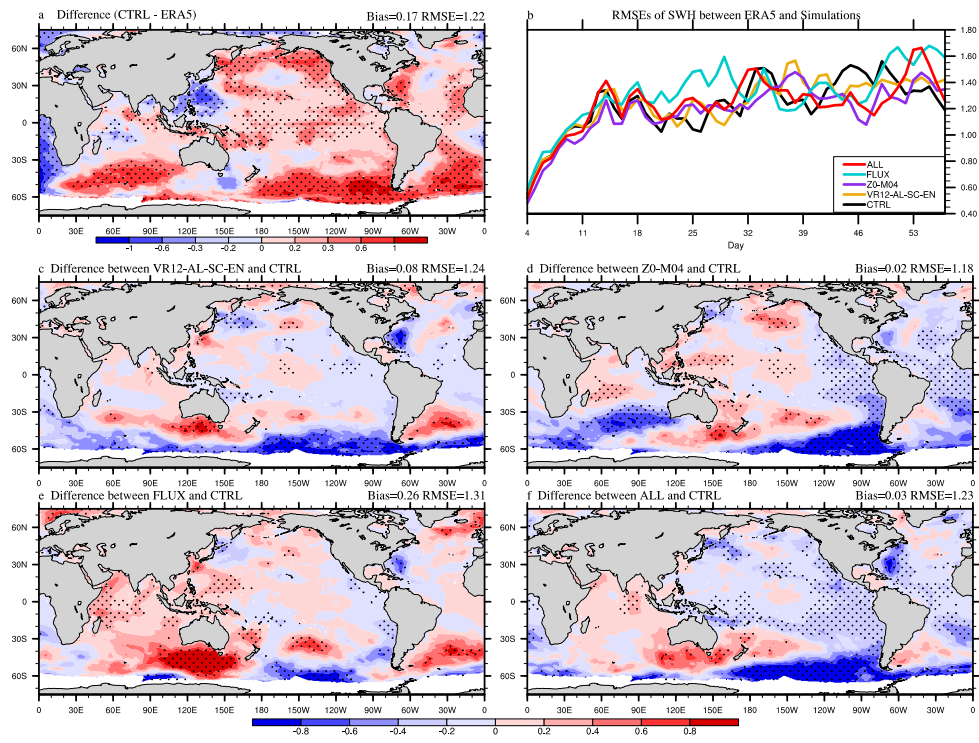
Figure 11. The same as Figure 10 but for Aug-Sep, 2018.
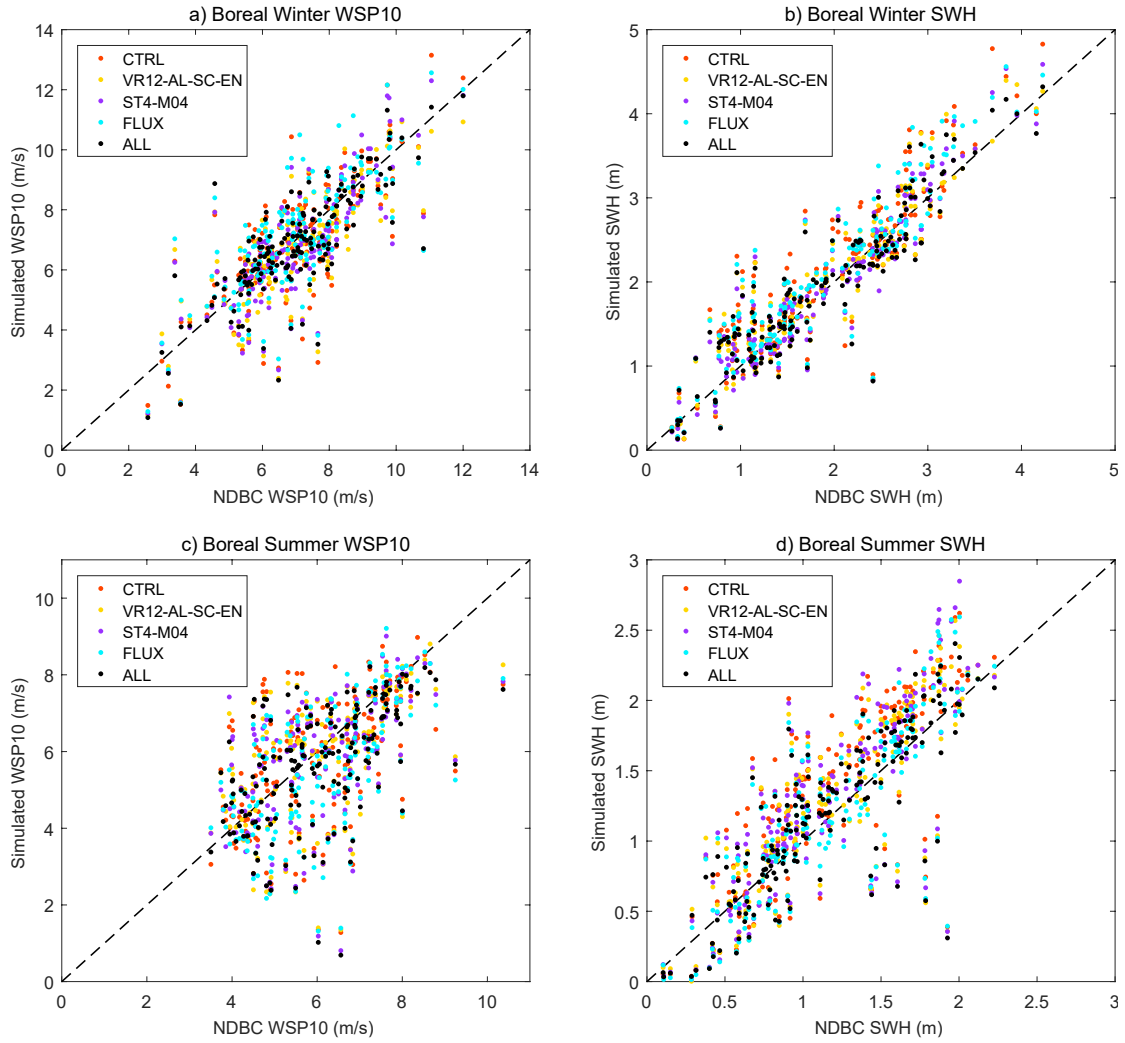
Figure 12. Scatter plots of simulated WSP10/SWH (y-axis) vs buoy WSP10/SWH (x-axis): (a) the WSP10 in Jan-Feb, 2017, (b) the SWH in Jan-Feb, 2017, (c) the WSP10 in Aug-Sep, 2018, and (d) the SWH in Aug-Sep, 2018. The dotted line is y=x. The corresponding mean biases with standard deviations and RMSEs for every experiment are shown in Table 2.